On the orientational dependence of drag experienced by spheroids

Pacha Sanjeevi, Sathish; Padding, Johan

DOI
10.1017/jfm.2017.239

Publication date
2017

Document Version
Accepted author manuscript

Published in
Journal of Fluid Mechanics

Citation (APA)
Pacha Sanjeevi, S., & Padding, J. (2017). On the orientational dependence of drag experienced by spheroids. *Journal of Fluid Mechanics*, *820*, Article R1. https://doi.org/10.1017/jfm.2017.239

JFM RAPIDS
journals.cambridge.org/rapids

On the orientational dependence of drag experienced by spheroids

Sathish K. P. Sanjeevi[1] and Johan T. Padding[1,2,]†

[1]Process and Energy Department, Delft University of Technology, Leeghwaterstraat 39, 2628 CB Delft, The Netherlands

[2]Department of Chemical Engineering and Chemistry, Eindhoven University of Technology, 5600 MB Eindhoven, The Netherlands

(Received xx; revised xx; accepted xx)

The flow around different prolate (needle-like) and oblate (disc-like) spheroids is studied using a multi-relaxation-time lattice Boltzmann method. We compute the mean drag coefficient $C_{D,\phi}$ at different incident angles ϕ for a wide range of Reynolds numbers (Re). We show that the sine-squared drag law $C_{D,\phi} = C_{D,\phi=0^\circ} + (C_{D,\phi=90^\circ} - C_{D,\phi=0^\circ})\sin^2\phi$ holds up to large Reynolds numbers $Re = 2000$. Further, we explore the physical origin behind the sine-squared law, and reveal that surprisingly, this does not occur due to linearity of flow fields. Instead, it occurs due to an interesting pattern of pressure distribution contributing to the drag at higher Re for different incident angles. The present results demonstrate that it is possible to perform just two simulations at $\phi = 0^\circ$ and $\phi = 90^\circ$ for a given Re and obtain particle shape specific C_D at arbitrary incident angles. However, the model has limited applicability to flatter oblate spheroids, which do not exhibit the sine-squared interpolation, even for $Re = 100$, due to stronger wake-induced drag. Regarding lift coefficients, we find that the equivalent theoretical equation can provide a decent approximation, even at high Re, for prolate spheroids.

1. Introduction

Industrial applications and real life cases often involve suspensions of non-spherical particles, of either regular or irregular shapes. Prolate (needle-like) spheroids can be used to describe milled biomass particles, fibrous suspensions, and submarine hulls. On the other hand, oblate (disc-like) particles can be approximated to represent red blood cells. El Khoury *et al.* (2010, 2012) performed direct numerical simulations (DNS) with the flow perpendicular to the spheroid's symmetry axis and investigated the wakes behind a prolate spheroid of ratio 6:1. Hölzer & Sommerfeld (2009) and Zastawny *et al.* (2012) investigated different non-spherical particles at different flow incident angles at different Re, albeit limiting mainly to the steady flow regime. Very recently, Ouchene *et al.* (2016) proposed force correlations for prolate spheroids upto aspect ratio of 32, again limited to steady flows with $Re \leqslant 240$. They report an interesting finding that the drag coefficient C_D of the prolate spheroids follows a sine-squared interpolation between its extreme C_D

† Email address for correspondence: J.T.Padding@tudelft.nl

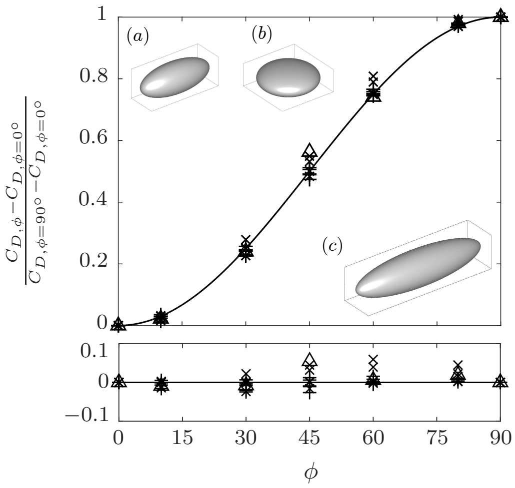

Figure 1: Top: The normalized drag coefficient $\frac{C_{D,\phi}-C_{D,\phi=0^\circ}}{C_{D,\phi=90^\circ}-C_{D,\phi=0^\circ}}$ plotted against incident angle ϕ. The solid line indicates $\sin^2\phi$. Data include (*a*) prolate spheroid (+) and (*b*) oblate spheroid (×), both of aspect ratio 5/2, both for *Re*=0.1, 10, 100, 1000 and 2000, (*c*) prolate spheroid of aspect ratio 4 (△) for *Re*=2000. Averaged C_D values are used for cases with vortex shedding occurring at high *Re*. Bottom: Difference between normalized drag coefficient and $\sin^2\phi$.

values for $Re \leqslant 240$ for the reported aspect ratios. In this paper, we investigate this phenomenon more deeply and to higher *Re*.

Some authors define the Reynolds number Re_d based on the minimum thickness of the particle d_{min}. For this work, the Reynolds number is defined as $Re = |\boldsymbol{u}_\infty| d_{eq}/\nu$, where $\boldsymbol{u}_\infty$ is the uniform inlet velocity, ν is the kinematic viscosity of the fluid, and d_{eq} is the diameter of the volume-equivalent sphere given by $d_{eq} = (6V_p/\pi)^{1/3}$ with V_p being the particle volume. The drag coefficient is defined as $C_D = |\boldsymbol{F}_D|/(\frac{1}{2}\rho|\boldsymbol{u}_\infty|^2\frac{\pi}{4}d_{eq}^2)$. Here, $\boldsymbol{F}_D$ is the drag force acting on the particle and ρ is the fluid density. For any particle in the Stokes regime (Happel & Brenner 1983), based on linearity of the Stokes equations, the drag coefficient at different incident angles ϕ interpolates as

$$C_{D,\phi} = C_{D,\phi=0^\circ} + (C_{D,\phi=90^\circ} - C_{D,\phi=0^\circ})\sin^2\phi. \tag{1.1}$$

Here, the subscript ϕ implies the value at that particular incident angle ϕ.

To motivate the reader, the drag on different spheroids is tested upto $Re = 2000$ and the mean C_D are plotted in figure 1. Surprisingly, the investigated particles follow sine-squared interpolation very well for both steady and unsteady regimes, even for *Re* as high as 2000. This interesting phenomenon appears to be similar to the Stokes regime prediction (equation 1.1) as mentioned by Ouchene *et al.* (2016). We investigated the phenomenon in detail and found a plausible reason and also the limitations of the sine-squared behaviour. Our findings at high *Re*, in combination with observations of Ouchene *et al.* (2016) for prolate spheroids upto aspect ratio 32, extends the validity of the drag law to both high aspect ratio prolate spheroids and high *Re*. This implies that in many situations, the mean drag coefficient at any incident angle $C_{D,\phi}$ for a given *Re* can be obtained by just knowing two values: $C_{D,\phi=0^\circ}$ and $C_{D,\phi=90^\circ}$.

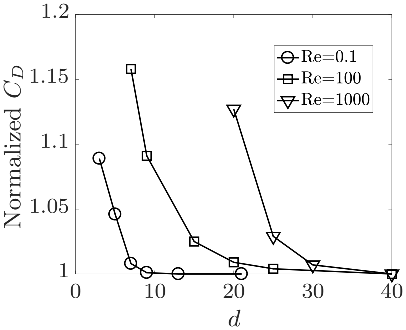

Figure 2: For a sphere, the normalized C_D as a function of diameter d in lattice cells for different Re, showing convergence of the method. The normalization is done with respect to the highest resolution C_D.

2. Numerical method

2.1. *Lattice Boltzmann method*

The fluid flow is simulated using a D3Q19, multi-relaxation time (MRT) lattice Boltzmann method (d'Humières *et al.* 2002). The MRT-LBM scheme solves the evolution of particle distribution function $|f\rangle$

$$|f(\boldsymbol{r}+\boldsymbol{e}_\alpha \varDelta t, t+\varDelta t)\rangle = |f(\boldsymbol{r},t)\rangle - \boldsymbol{M}^{-1}\hat{\boldsymbol{S}}(|m(\boldsymbol{r},t)\rangle - |m^{(eq)}(\boldsymbol{r},t)\rangle), \tag{2.1}$$

for position $\boldsymbol{r}$ with discrete velocities $\boldsymbol{e}_\alpha$ in directions $\alpha = 1, 2..., 19$. $\boldsymbol{M}$ is a 19×19 transformation matrix used to transform $|f\rangle$ from velocity space to moment space $|m\rangle$ with $|m\rangle = \boldsymbol{M} \cdot |f\rangle$. Here, the ket vector $|\cdot\rangle$ implies a column vector. The relaxation matrix $\hat{\boldsymbol{S}} = \boldsymbol{M} \cdot \boldsymbol{S} \cdot \boldsymbol{M}^{-1}$ is a 19×19 diagonal matrix. $\hat{\boldsymbol{S}}$ utilizes different, optimally chosen relaxation rates for different moments, thereby providing better stability compared to the single-relaxation-time LBM scheme (d'Humières *et al.* 2002). The matrices $\boldsymbol{M}$ and $\hat{\boldsymbol{S}}$ are similar to Huang *et al.* (2012). The kinematic viscosity of the fluid is set by the relaxation time τ as $\nu = c_s^2(\tau - 1/2)\varDelta t$, and the pressure p is related to the density by $p = \rho c_s^2$. Uniform velocity in the z-direction is prescribed at the inlet boundary based on Hecht & Harting (2010). The side walls are prescribed with free-slip boundaries rather than periodic boundary conditions, which could cause the flow to deflect either up or down based on inclination of the non-spherical particle (Hölzer & Sommerfeld 2009). The downstream (outlet) is specified with axial-stress-free boundary condition with $\partial u_z/\partial z = 0$ (Aidun *et al.* 1998). We use the linearly interpolated bounce back scheme (Bouzidi *et al.* 2001; Lallemand & Luo 2003) to accurately consider the curved geometry of the particle. The improvement in solution accuracy is negligible between linear and quadratic interpolation schemes, provided sufficient resolution is used (Pan *et al.* (2006); Kruggel-Emden *et al.* (2016)).

2.2. *Influence of grid resolution*

The influence of the grid resolution is tested with the flow around an isolated sphere. The normalized C_D is plotted in figure 2. Three different regimes are tested (i) Stokes flow, (ii) intermediate Reynolds number at $Re = 100$ with a steady wake, and (iii) high Reynolds number $Re = 1000$ exhibiting a complex, unsteady wake and therefore the *mean* drag coefficient is shown. The influence of the resolution is stronger with increasing Re as seen in figure 2. For $Re = 1000$, the observed C_D at resolution $d_{eq} = 40$ is 0.456 and is in good agreement with literature results: $C_D = 0.464$ from Vakarelski *et al.* (2016)

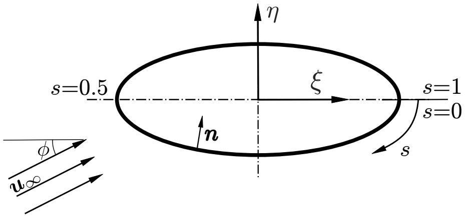

Figure 3: The local coordinate system (ξ,η) of the ellipsoidal section. s is the normalized distance along the circumference. $\boldsymbol{n}$ is the inward facing, local unit normal vector. The simulations are performed in a rectangular domain with particle rotated for different incident angles. For clarity and consistency, the results are analysed in the local coordinate system of the section (ξ,η).

and $C_D = 0.48$ from Ploumhans *et al.* (2002). This resolution information is considered in maintaining the minimum thickness d_{min} of our non-spherical particles at different Re. Due to the non-sphericity, the other dimension is always larger than the minimum thickness and therefore a good particle resolution is ensured.

3. Test of linearity for pressure and velocity fields

The drag law for Stokes flow (equation 1.1) for non-spherical particles is based on the linearity of the Stokes equations in the creeping flow limit. As figure 1 shows, we observe that the mean C_D follows the same sine-squared behaviour even in regimes with a complex unsteady wake at Re as high as 2000. It has to be noted that all the investigated geometries are axi-symmetric, smooth and rounded. Though non-linear effects dominate at higher Re, we first investigate if the inherent smooth nature of the geometries results in cancellation of non-linearity effects in the region close to the particle surface. In other words, we test whether the velocity and pressure fields for an arbitrary particle at incident angle ϕ obey the following conditions sufficiently close to the surface:

$$\boldsymbol{u}_\phi = \boldsymbol{u}_{\phi=0^\circ}\cos\phi + \boldsymbol{u}_{\phi=90^\circ}\sin\phi, \tag{3.1}$$

$$p_\phi - p_\infty = (p_{\phi=0^\circ} - p_\infty)\cos\phi + (p_{\phi=90^\circ} - p_\infty)\sin\phi. \tag{3.2}$$

Here, $\boldsymbol{u}_\phi$ is the velocity field and p_ϕ is the pressure field around the particle, based on the incoming flow $\boldsymbol{u}_\infty$ oriented at angle ϕ, as shown in figure 3. If equations 3.1 and 3.2 are true, the corresponding drag components, i.e. the viscous drag $C_{D\nu,\phi}$ and the pressure drag $C_{Dp,\phi}$, also follow the sine-squared law.

Throughout this paper, from the *three-dimensional* simulations, the flow fields are analysed along the meridional plane. The meridional plane contains the axis of symmetry of the particle at different incident angles and the inflow velocity vector $\boldsymbol{u}_\infty$. Of the different particles tested, we consider the prolate spheroid of aspect ratio 5/2 for the linearity study. A special case of $\phi = 30^\circ$ is tested along the meridional plane. The velocity and pressure fields from the theoretical linear combination in equations 3.1 and 3.2 are compared with the actual flow field from the simulations. Two cases, one for the Stokes flow at $Re = 0.1$ and another exhibiting steady flow, yet sufficiently large Re compared to the Stokes regime, $Re = 100$, are considered. The velocity fields based on the theory and the actual flow are given in figure 4. For Stokes flow, the linear superposition of velocity fields result in attached flow around the particle. There is a good match between the theoretical and actual fields with deviations upto 2%. At $Re = 100$, the flow field exhibits attached flow for $\phi = 0^\circ$ due to streamlining and a strong recirculation for $\phi = 90^\circ$. In figure 4(d), the linear combination of them for $\phi = 30^\circ$ still appears attached,

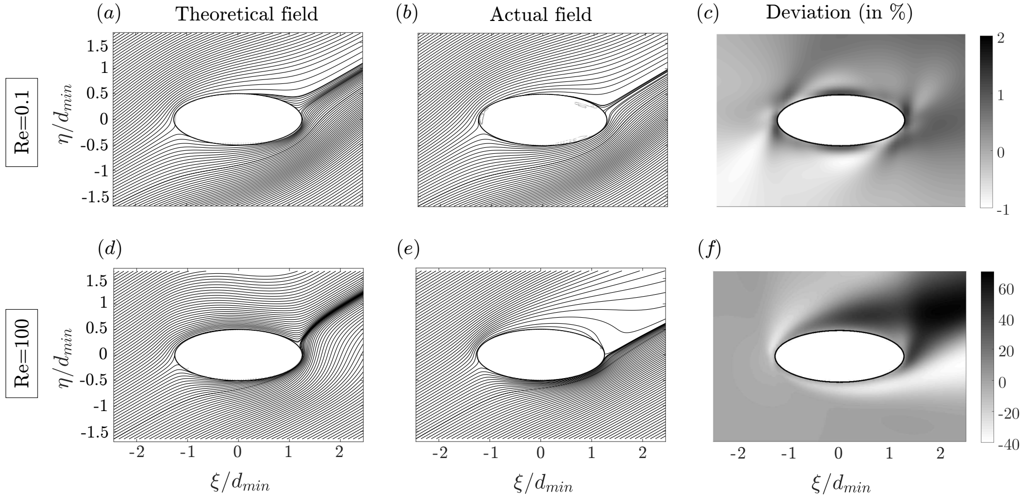

Figure 4: The theoretical and actual velocity fields and the deviation between these fields for $Re = 0.1$ (a, b, c) and $Re = 100$ (d, e, f), respectively. The deviation is computed as $\frac{\|\boldsymbol{u}_{th} - \boldsymbol{u}_{act}\|}{\|\boldsymbol{u}_\infty\|}$ in %. Note the deviation scales are different for different Re.

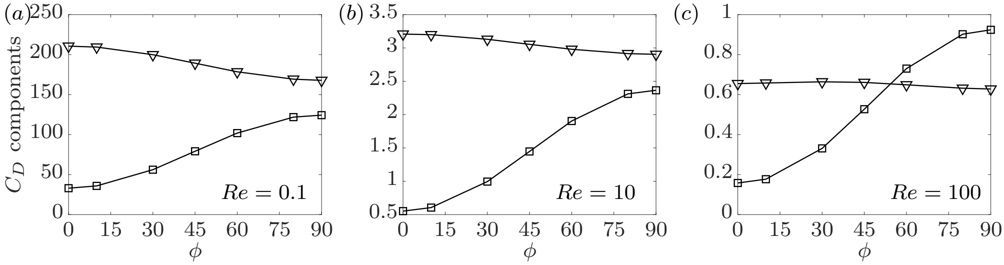

Figure 5: ($\triangledown$) Viscous and ($\square$) pressure components of the drag coefficient as a function of incident angle ϕ at (a) $Re = 0.1$, (b) $Re = 10$, and (c) $Re = 100$.

whereas the actual flow field as shown in figure 4(e) exhibits recirculation in the wake of the particle. There is a strong mismatch between the fields, as shown in figure 4(f) with deviations upto 60%.

At the same time, it is interesting to note that the viscous drag force resulting from the velocity field becomes increasingly independent of incident angle ϕ at higher Re. Figure 5 shows the viscous and pressure drag components at Re=0.1, 10 and 100 for the prolate spheroid of aspect ratio 5/2. Indeed, it is observed that the viscous effects become weakly dependent on incident angle ϕ at $Re = 10$. Eventually at $Re = 100$, the viscous drag becomes independent of ϕ compared to change in the pressure drag, with $C_{D\nu,\phi} \approx C_{D\nu,\phi=0^\circ} \approx C_{D\nu,\phi=90^\circ}$. This implies that the dependence of the drag on the particle's incident angle ϕ, at higher Re, is purely coupled to the ϕ-dependence of the pressure drag. Therefore, we next focus on the pressure coefficient on the surface of the meridional plane section.

The pressure coefficient is defined as $C_p = (p - p_\infty)/(1/2\rho|\boldsymbol{u}_\infty|^2)$ with pressure p measured on the surface and p_∞ the pressure at the far field. C_p is plotted as a function of the distance s along the circumference of the meridional section, normalized with the section circumference, as shown in figure 3. The C_p distributions on the section along the spheroid's meridional plane are plotted for $Re = 0.1$ and $Re = 100$ in figures 6(a) and

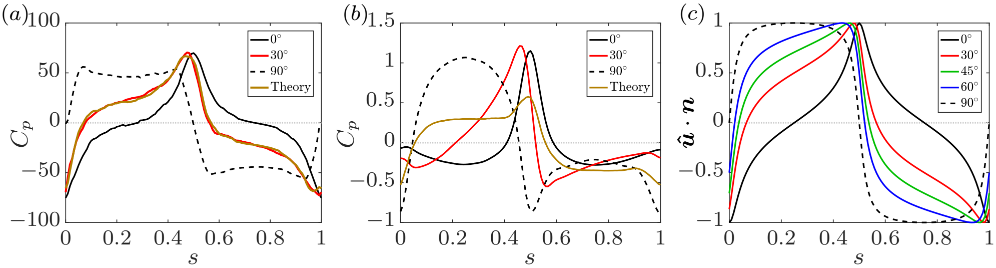

Figure 6: Distribution of C_p against normalized distance s along the circumference of the meridional section for (*a*) $Re = 0.1$ and (*b*) $Re = 100$; (*c*) surface normal projections $\hat{\boldsymbol{u}} \cdot \boldsymbol{n}$ for different incident angles ϕ. Note the linearity theory matches perfectly with simulations for $Re = 0.1$ and shows strong mismatch for $Re = 100$. For the different ϕ shown, note the matching trends of C_p at $Re = 0.1$ with $\hat{\boldsymbol{u}} \cdot \boldsymbol{n}$.

(*b*), respectively. Referring to figure 3, the $\boldsymbol{u}_\infty$ at $\phi = 0°$ is along the $+\xi$ axis and the C_p peaks are observed near $s = 0.5$ in figures 6(*a*) and (*b*), which is at the leading edge of the spheroid for that incident angle. At $Re = 0.1$, we observe an exact match between C_p using the linearity theory (equation 3.2) and the actual simulation for $\phi = 30°$. At $Re = 100$, the actual C_p distribution for $\phi = 30°$ is different compared to the distribution based on linearity theory as seen in figure 6(b). Therefore, it can be concluded that it is not due to linearity that the drag law shows sine-squared behaviour at higher Re.

4. Reason for sine-squared drag law at higher *Re*

Again we consider the meridional section of the prolate spheroid of aspect ratio 5/2 for this study. We hypothesize that the C_p distribution takes the form

$$C_p = -m + (1+m)(\hat{\boldsymbol{u}} \cdot \boldsymbol{n})^k. \tag{4.1}$$

Here, m and k are constants, $\hat{\boldsymbol{u}} = \boldsymbol{u}_\infty / |\boldsymbol{u}_\infty|$ is the orientation of the far-field flow direction, and $\boldsymbol{n}$ is the inward facing local unit normal vector, as in figure 3. The above form $-m + (1+m)(\hat{\boldsymbol{u}} \cdot \boldsymbol{n})^k$ is inspired from the inviscid flow around a sphere, where $C_p = 1 - c \sin^2\theta$ with $c = 9/4$ and the θ measured from the stagnation point. For a sphere, $\hat{\boldsymbol{u}} \cdot \boldsymbol{n} = \cos\theta$ and rearranging terms with $m = c - 1$, the C_p distribution for a sphere becomes $C_p = -m + (1+m)(\hat{\boldsymbol{u}} \cdot \boldsymbol{n})^2$. A more general form is considered in our case with an arbitrary exponent k.

The term $-m$ acts as a negative offset and the term $(1+m)$ acts as a scaling factor, such that $C_p = 1$ at the stagnation point ($\hat{\boldsymbol{u}} \cdot \boldsymbol{n} = 1$), as would be expected from Bernoulli's law at the point where $\boldsymbol{u} = \boldsymbol{0}$. For increasing Re, the high pressure region localizes more around the stagnation point and this can be confirmed by comparing the C_p distribution for $\phi = 0°$ at Re=0.1 and 100 in figure 6(*a*) and (*b*), respectively. Also for $Re >> 1$, figures 7(*a*) and (*b*) show that the dominant part of the pressure drag originates from the particle's front side ($\hat{\boldsymbol{u}} \cdot \boldsymbol{n} > 0$, see figure 6(*c*)) and therefore we focus on this region. For $Re >> 1$, we choose $k = 2$. The value $k = 2$ is inspired by inviscid irrotational flow theory as discussed above, although the flow is not exactly inviscid. The distributions of C_p for $Re = 100$, $Re = 2000$ (time averaged), and $(\hat{\boldsymbol{u}} \cdot \boldsymbol{n})^2 \mathcal{H}(\hat{\boldsymbol{u}} \cdot \boldsymbol{n})$ are given in figures 7(*a*), (*b*) and (*c*) respectively. Here, $\mathcal{H}$ is the Heaviside step function given by

$$\mathcal{H}(x) = \begin{cases} 1 & \text{if } x > 0, \\ 0 & \text{otherwise.} \end{cases} \tag{4.2}$$

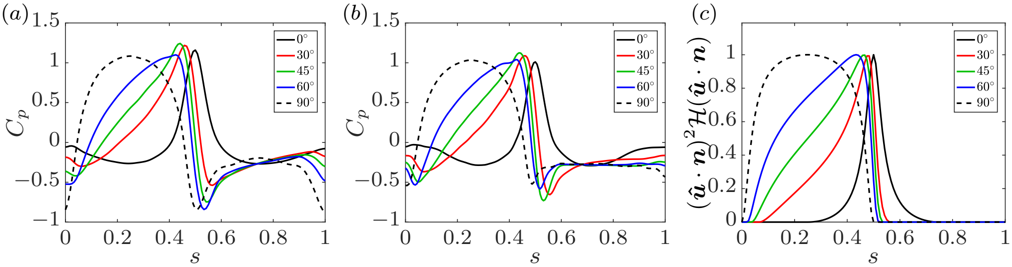

Figure 7: Distributions of C_p at (a) $Re = 100$, (b) $Re = 2000$ (time averaged), and (c) second power surface normal projections $(\hat{\boldsymbol{u}}\cdot\boldsymbol{n})^2\mathcal{H}(\hat{\boldsymbol{u}}\cdot\boldsymbol{n})$ versus the normalized distance s along the circumference of the meridional section for different ϕ.

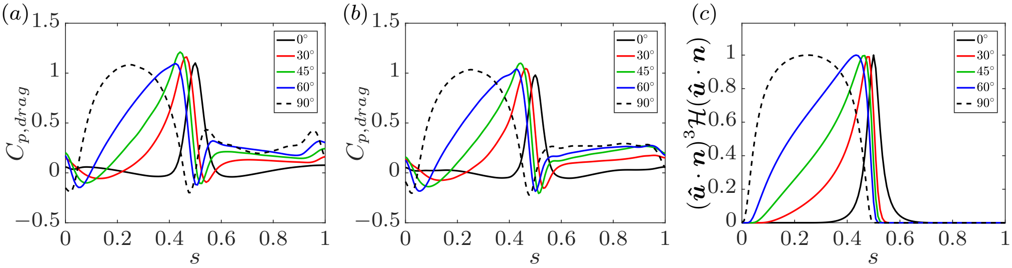

Figure 8: Distributions of $C_{p,drag}$ at (a) $Re = 100$, (b) $Re = 2000$ (time averaged), and (c) third power surface normal projections $(\hat{\boldsymbol{u}}\cdot\boldsymbol{n})^3\mathcal{H}(\hat{\boldsymbol{u}}\cdot\boldsymbol{n})$ versus the normalized distance s along the circumference of the meridional section for different ϕ.

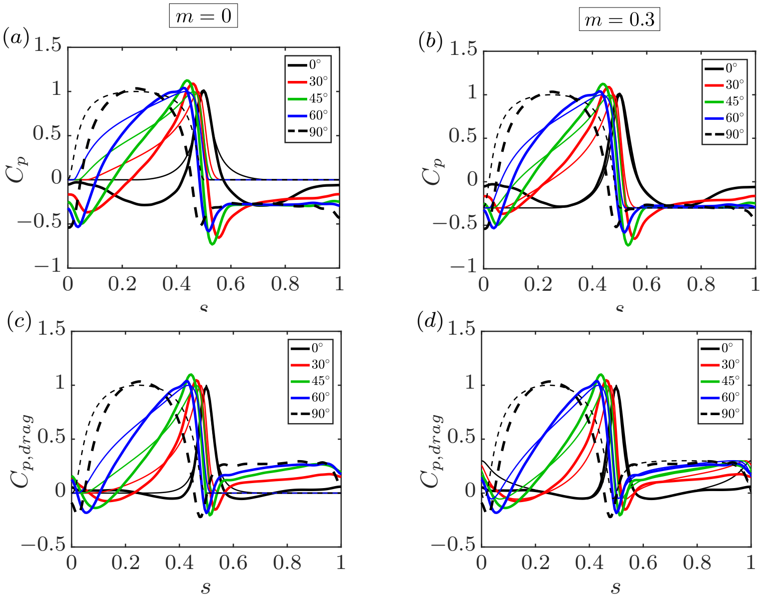

Figure 9: Quantitative comparison of the C_p (a,b) and $C_{p,drag} = C_p\hat{\boldsymbol{u}}\cdot\boldsymbol{n}$ (c,d) from the proposed theory (equation 4.1, thin lines) with the actual measurements at $Re = 2000$ (thick lines). We used $m = 0$ (a,c) and $m = 0.3$ (b,d), respectively. Note that the influence of the value of m is weaker for $C_{p,drag}$ compared to C_p.

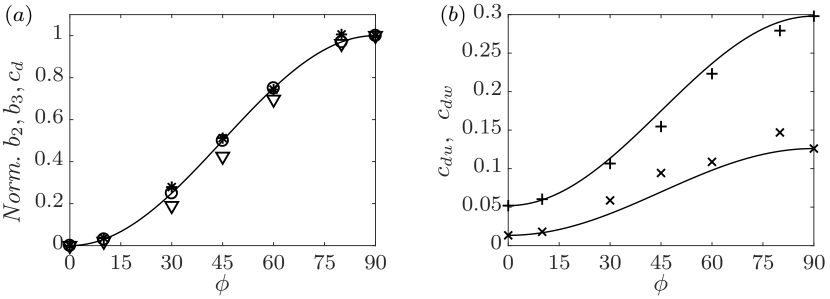

Figure 10: For a prolate spheroid of aspect ratio 5/2: (*a*) the normalized $b_{2,\phi}$ (○), $b_{3,\phi}$ (▽), sectional pressure drag $c_{d,\phi}$ at $Re = 2000$ ($*$), and $\sin^2\phi$ (solid line); (*b*) components of sectional pressure drag $c_{d,\phi}$ at $Re = 2000$ decomposed into upstream drag $c_{du,\phi}$ (+) and wake side drag $c_{dw,\phi}$ (×), together with their corresponding sine-squared interpolating curves. Note that the trends of $b_{3,\phi}$ and $c_{du,\phi}$ are similar, both under their respective sine-squared curves.

The term $\mathcal{H}(\hat{\boldsymbol{u}} \cdot \boldsymbol{n})$ is introduced above to consider only the front side of the particle projected to the inflow.

It can be observed that the maximum values of C_p for different ϕ are nearly the same and close to 1, as expected at the stagnation point in inviscid flow. Also, the overall trend of the C_p curves in figures 7(*a*) and (*b*), and the $(\hat{\boldsymbol{u}} \cdot \boldsymbol{n})^2\mathcal{H}(\hat{\boldsymbol{u}} \cdot \boldsymbol{n})$ in figure 7(*c*) are almost similar, including the trends of curvature. Actually for the pressure drag, we specifically need to look at the surface projection of C_p along the flow direction, i.e. $C_{p,drag} = C_p\hat{\boldsymbol{u}} \cdot \boldsymbol{n}$. The similarity between $C_{p,drag}$ and $(\hat{\boldsymbol{u}} \cdot \boldsymbol{n})^3$ for different angles can be observed in figures 8(*a*), (*b*) and (*c*). The trends agree well for different incident angles. Further, the C_p and $C_{p,drag}$ distributions for $Re = 100$ and $Re = 2000$ indicate that they are self-similar and independent of Re, at least for the front side of the particle $(\hat{\boldsymbol{u}} \cdot \boldsymbol{n} > 0)$. Note that the influence of the offset m is less significant for $C_{p,drag}$ than it is for C_p. Also, the precise value of m may be position and incident angle dependent, but its variation is negligible compared to the overall variation in the pressure drag. This is shown explicitly in figure 9, where the measured C_p distributions are compared with our proposed C_p form computed as: $C_p = -m + (1+m)(\hat{\boldsymbol{u}} \cdot \boldsymbol{n})^2\mathcal{H}(\hat{\boldsymbol{u}} \cdot \boldsymbol{n})$ and the $C_{p,drag}$ accordingly. It can be observed that the value m influences C_p considerably. However, its influence on $C_{p,drag}$ is much weaker and therefore, we proceed with $m = 0$ in upcoming steps.

$C_{p,drag}$ corresponds to the local contribution of pressure to the sectional pressure drag. Therefore, we require integrals to compute the total pressure drag due to this section. We define the integral of k^{th} power of projection $\hat{\boldsymbol{u}} \cdot \boldsymbol{n}$ for the front side of the section as

$$b_k = \int_0^1 (\hat{\boldsymbol{u}} \cdot \boldsymbol{n})^k \mathcal{H}(\hat{\boldsymbol{u}} \cdot \boldsymbol{n})\, ds. \tag{4.3}$$

An interesting property is that the integral of the second power of projection, b_2, exactly obeys sine-squared behaviour for different ϕ. This can be written as $b_{2,\phi} = b_{2,\phi=0^\circ} + (b_{2,\phi=90^\circ} - b_{2,\phi=0^\circ})\sin^2\phi$ and is shown in figure 10(*a*). This law holds for the family of ellipsoidal sections and is independent of aspect ratio. This can also be confirmed from the fact that the C_p distribution is proportional to $\hat{\boldsymbol{u}} \cdot \boldsymbol{n}$ in Stokes flow (see figures 6(*a*) and (*c*)) and therefore $C_{p,drag} = C_p\hat{\boldsymbol{u}} \cdot \boldsymbol{n}$ is proportional to $(\hat{\boldsymbol{u}} \cdot \boldsymbol{n})^2$.

As per our earlier observation, at higher Re, the $C_{p,drag}$ distribution is proportional

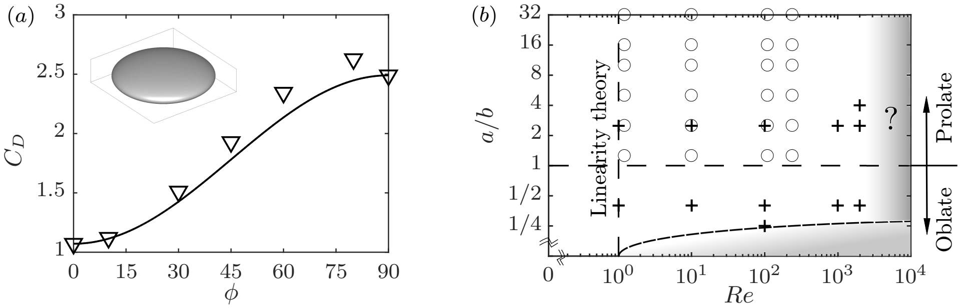

Figure 11: (a) C_D against ϕ at $Re = 100$ for oblate spheroid of aspect ratio 4 ($\triangledown$) and the corresponding sine-squared interpolating curve (solid line), (b) the tested data points ($+$) and the *plausible* valid region for sine-squared scaling (unshaded). The valid region is based on our results and the data of Ouchene *et al.* (2016) for prolate spheroids upto aspect ratios 32 and $Re = 240$ ($\circ$). The ratio a/b is the ratio of lengths parallel and orthogonal to the axis of rotation.

to $(\hat{\boldsymbol{u}} \cdot \boldsymbol{n})^3$. However, the integral $b_{3,\phi}$ does not exactly hold sine-squared behaviour, as shown in figure 10(a). It trends slightly below the sine-squared curve. The equivalent of $b_{3,\phi}$ is the sectional pressure drag from the upstream side of the section, which we compare in the upcoming steps. We define sectional pressure drag integrated over the circumference of an ellipsoidal section as

$$c_d = \int_0^1 C_{p,drag}\, ds. \tag{4.4}$$

We then decompose c_d into upstream side (c_{du}) and wake side (c_{dw}), respectively, as

$$c_{du} = \int_0^1 C_{p,drag}\mathcal{H}(\hat{\boldsymbol{u}} \cdot \boldsymbol{n})\, ds, \quad \text{and} \quad c_{dw} = \int_0^1 C_{p,drag}\mathcal{H}(-\hat{\boldsymbol{u}} \cdot \boldsymbol{n})\, ds.$$

The above integrals for different incident angles ϕ, i.e. $c_{du,\phi}$ and $c_{dw,\phi}$, for $Re = 2000$ are plotted in figure 10(b) and their corresponding sine-squared interpolation curves based on the end values. As seen from figures 10(a) and (b), the upstream drag $c_{du,\phi}$ trend is very similar to $b_{3,\phi}$ and both are slightly below their respective sine-squared curves. At the same time, the wake induced drag component $c_{dw,\phi}$ values are slightly above their respective sine-squared curve at the intermediate angles, i.e. $0° < \phi < 90°$. Therefore, the wake drag adequately compensates the upstream drag proportionately at the intermediate angles and thereby making the total section drag appear to scale in a sine-squared manner. The normalized, sectional pressure drag $c_{d,\phi}$ for different angles for $Re = 2000$ itself follows near sine-squared pattern as shown in figure 10(a). The spheroid by itself is made of different such ellipsoidal sections, each obeying sine-squared behaviour of different scales and altogether giving the total drag sine-squared behaviour. We have tested the reasoning in this section for different aspect ratio prolate spheroids, and found similar dependencies of $C_{p,drag}$ with $(\hat{\boldsymbol{u}} \cdot \boldsymbol{n})^3\mathcal{H}(\hat{\boldsymbol{u}} \cdot \boldsymbol{n})$ for different ϕ.

4.1. *Limitations and comments*

In the introduction, we showed results of prolate spheroids of different aspect ratios and an oblate spheroid of ratio 5/2. However, increasing the aspect ratio for an oblate spheroid results in an increasing digression from the sine-squared drag law, even at moderate Re. The C_D results of oblate spheroid of aspect ratio 4 at $Re = 100$ are presented in figure

11(a). Clearly, a non-monotonic dependence of C_D on the incidence angle ϕ is observed. The observed maximum deviation is around 10% at $\phi = 60^\circ$ against the sine-squared curve. The reason why the drag law fails for flatter discs can be explained from our earlier observation that the wake has a higher drag contribution at intermediate angles $0^\circ < \phi < 90^\circ$ (see c_{dw} in figure 10(b)), when compared with the sine-squared curve. The flat-disc like geometry experiences a stronger wake, amplifying the effect strongly. If we assume a 10% deviation to be the limit of applicability, the oblate spheroid of aspect ratio 4 is at the bounding limit for the drag law. On the other hand, prolate spheroids of larger aspect ratio, as shown in the introduction, still obey the sine-squared behaviour even at $Re = 2000$, due to the weaker wake side drag. A sketch of the *plausible* valid region of the sine-squared behaviour is shown in figure 11(b). We have also tested a capsule-like spherocylinder of aspect ratio 4 and it also exhibits sine-squared drag scaling at high Re, due to closer resemblance to prolate spheroid. The C_D results from this work will be published as correlations dependent of Re and ϕ in a separate paper. Since the prolate spheroid of aspect ratio 4 is simulated only for $Re = 2000$, the corresponding results are given here, with $C_{D,\phi=0^\circ} = 0.147$ and $C_{D,\phi=90^\circ} = 1.105$.

The $Re = 2000$ limit for the tested particles is rather limited by the LBM solver and not by the flow physics itself. We believe that the drag law might hold to even higher Re. However, flow fields are indeed complex for high Re and the extent to which the drag law is valid needs further investigation. For example, Jiang *et al.* (2015) simulated flow around a 6:1 prolate spheroid at $\phi = 45^\circ$ at $Re = 3000$ based on minor diameter. They reported a side force, almost 75% in magnitude of the drag force, perpendicular to the meridional plane. This indicates the flow is highly asymmetric about the meridional plane. However, they do not investigate the incident angle dependence of the drag force. To which extent their reported flow asymmetries might influence the sine-squared drag behaviour is not yet known and therefore needs further investigation.

5. Lift forces

Besides drag, any non-spherical particle at an inclination with respect to a uniform flow will experience lift. Here, we provide a concise section with interesting observations and comments regarding the lift forces.

We define the lift coefficient as $C_L = |\boldsymbol{F}_L|/(\frac{1}{2}\rho|\boldsymbol{u}_\infty|^2\frac{\pi}{4}d_{eq}^2)$ with F_L being the measured lift force. For a particle in the Stokes regime, based on linearity theory, the C_L at an incident angle ϕ is

$$C_{L,\phi} = (C_{D,\phi=90^\circ} - C_{D,\phi=0^\circ})\sin\phi\cos\phi. \tag{5.1}$$

From our experience of the different non-spherical particles tested, equation 5.1 is still a *decent approximation* in the complete absence of C_L data for prolate spheroids, even at high Re, as seen in figure 12(a). The average of the absolute deviations between $C_{L,\phi}$ from the simulations and the equation 5.1 is less than 15% for the tested prolate spheroids at different Re. For oblate spheroids, with increasing aspect ratios, the deviations increase more, as seen in figure 12(b). For the oblate spheroid of aspect ratio 4 at $Re = 100$, the simulated C_L is much larger, by around 60%, than the theory for the reasons already observed in figure 10(b). Similar to the drag, the wake induced force is also contributing strongly to the lift and thereby making the observed C_L much larger than the theory at intermediate incident angles.

There are different reasons the incident angle dependence of the lift coefficient C_L cannot be *exactly* quantified in a predictable fashion like that of C_D. The lift coefficient's order of magnitude depends on the difference of C_D at two extreme incident angles, i.e.

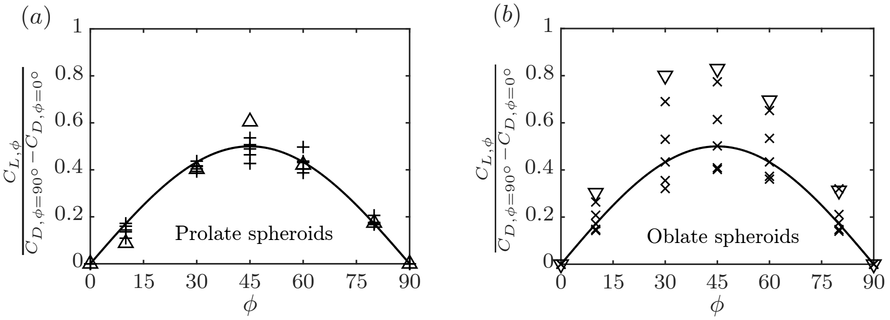

Figure 12: The normalized lift coefficient $\frac{C_{L,\phi}}{C_{D,\phi=90^\circ}-C_{D,\phi=0^\circ}}$ plotted against incident angle ϕ. The solid line indicates $\sin\phi\cos\phi$. (*a*) prolate spheroid of aspect ratio 5/2 for Re=0.1, 10, 100, 1000 and 2000 (+); prolate spheroid of aspect ratio 4 at Re=2000 (△), and (*b*) oblate spheroid of aspect ratio 5/2 for Re=0.1, 10, 100, 1000 and 2000 (×); oblate spheroid of aspect ratio 4 at $Re = 100$ (▽). Note that the oblate spheroids are experiencing stronger deviations compared to prolate spheroids.

$(C_{D,\phi=90^\circ} - C_{D,\phi=0^\circ})$ and goes to zero at the extreme ends of incident angles, i.e. at $\phi = 0^\circ, 90^\circ$. However for C_D at different incident angles ϕ, apart from the C_D difference term, there is an additional term giving a constant offset, i.e. C_D at $\phi = 0^\circ$. This implies that the variation of $C_{L,\phi}$ is much more sensitive than that of $C_{D,\phi}$. Therefore, any variation in pressure distribution at higher Re would be more amplified for C_L than for C_D. The C_L results from this work will be published as correlations dependent of Re and ϕ in a separate paper.

6. Conclusion

The flow around prolate and oblate spheroids of different aspect ratios was studied. We explored the sine-squared drag law in detail with a prolate spheroid of aspect ratio 5/2. We found that the reason for the drag law at high Re is not due to linearity theory, which results in an identical drag law in the Stokes regime. At high Re, the viscous drag becomes almost independent of incident angle ϕ and the pressure drag is the only factor influenced by incident angle ϕ. At high Re, the pressure distribution contributing to the drag shows a dependency of the surface normal's orientation with the incoming flow in a consistent pattern as discussed. Prolate spheroids of higher aspect ratios follow the sine-squared pattern even at $Re = 2000$. Oblate spheroids of aspect ratio 4 or larger do not exhibit sine-squared pattern due to strong wake induced drag. Regarding lift coefficients, we find that the theoretical C_L equation can provide a decent approximation, even at high Re, for prolate spheroids.

Both the drag law, valid at high Re for the prolate spheroids and low aspect ratio oblate spheroids, and the lift law for the prolate spheroids, hold good potential for different applications. For example, they are very useful for Euler-Lagrangian flow simulations of non-spherical particles. Any particle shape-specific C_D and C_L for a given Re at different ϕ, even at high Re, can be obtained by performing just two simulations: C_D at $\phi = 0^\circ$ and $\phi = 90^\circ$.

Acknowledgements

The authors thank the European Research Council for its financial support under its consolidator grant scheme, contract no. 615906 (NonSphereFlow). The simulations are performed in LB3D code with additional improvements. We thank Prof. Jens Harting for providing the code and Prof. Hans Kuipers for the fruitful discussions. The first author thanks Dr. Ahad Zarghami and Qingguang Xie for the interesting discussions on LBM. The work has been made possible by a grant for computation time, project number SH-351-15, financed by the Netherlands Organisation for Scientific Research (NWO).

References

Aidun, C. K., Lu, Y., Ding, E.-J. & others 1998 Direct analysis of particulate suspensions with inertia using the discrete Boltzmann equation. *J. Fluid Mech.* **373**, 287–311.

Bouzidi, M., Firdaouss, M. & Lallemand, P. 2001 Momentum transfer of a Boltzmann-lattice fluid with boundaries. *Phys. Fluids* **13**, 3452–3459.

d'Humières, D., Ginzburg, I., Krafczyk, M., Lallemand, P. & Luo, L.-S. 2002 Multiple–relaxation–time lattice Boltzmann models in three dimensions. *Phil. Trans. R. Soc. Lond. A* **360**, 437–451.

El Khoury, G. K., Andersson, H. I. & Pettersen, B. 2010 Crossflow past a prolate spheroid at Reynolds number of 10000. *J. Fluid Mech.* **659**, 365–374.

El Khoury, G. K., Andersson, H. I. & Pettersen, B. 2012 Wakes behind a prolate spheroid in crossflow. *J. Fluid Mech.* **701**, 98–136.

Happel, J. & Brenner, H. 1983 *Low Reynolds number hydrodynamics: with special applications to particulate media*, , vol. 1. Springer Science & Business Media.

Hecht, M. & Harting, J. 2010 Implementation of on-site velocity boundary conditions for D3Q19 lattice Boltzmann simulations. *J. Stat. Mech. Theor. Exp.* **2010**, P01018.

Hölzer, A. & Sommerfeld, M. 2009 Lattice Boltzmann simulations to determine drag, lift and torque acting on non-spherical particles. *Comput. Fluids* **38**, 572–589.

Huang, H., Yang, X., Krafczyk, M. & Lu, X.-Y. 2012 Rotation of spheroidal particles in Couette flows. *J. Fluid Mech.* **692**, 369–394.

Jiang, F., Gallardo, J. P., Andersson, H. I. & Zhang, Z. 2015 The transitional wake behind an inclined prolate spheroid. *Phys. Fluids* **27**, 093602.

Kruggel-Emden, H., Kravets, B., Suryanarayana, M. K. & Jasevicius, R. 2016 Direct numerical simulation of coupled fluid flow and heat transfer for single particles and particle packings by a LBM-approach. *Powder Technol.* **294**, 236–251.

Lallemand, P. & Luo, L.-S. 2003 Lattice Boltzmann method for moving boundaries. *J. Comput. Phys.* **184**, 406–421.

Ouchene, R., Khalij, M., Arcen, B. & Tanière, A. 2016 A new set of correlations of drag, lift and torque coefficients for non-spherical particles and large Reynolds numbers. *Powder Technol.* **303**, 33–43.

Pan, C., Luo, L.-S. & Miller, C. T. 2006 An evaluation of lattice Boltzmann schemes for porous medium flow simulation. *Comput. Fluids* **35**, 898–909.

Ploumhans, P., Winckelmans, G. S., Salmon, J. K., Leonard, A. & Warren, M. S. 2002 Vortex methods for direct numerical simulation of three-dimensional bluff body flows: application to the sphere at Re= 300, 500, and 1000. *J. Comput. Phys.* **178**, 427–463.

Vakarelski, I. U., Berry, J. D., Chan, D. Y. C. & Thoroddsen, S. T. 2016 Leidenfrost vapor layers reduce drag without the crisis in high viscosity liquids. *Phys. Rev. Lett.* **117**, 114503.

Zastawny, M., Mallouppas, G., Zhao, F. & Van Wachem, B. 2012 Derivation of drag and lift force and torque coefficients for non-spherical particles in flows. *Int. J. Multiph. Flow* **39**, 227–239.